

Continental-scale surface reflectance product from CBERS-4 MUX data: Assessment of atmospheric correction method using coincident Landsat observations

Vitor S. Martins ^{a,b*}, João V. Soares ^c, Evlyn M. L. M. Novo ^d, Claudio C. F. Barbosa ^b, Cibele T. Pinto ^e, Jeferson S. Arcanjo ^b, Amy Kaleita ^a.

^a Agricultural and Biosystems Engineering, Iowa State University (ISU), Ames, IA, United States.

^b Image Processing Division, National Institute for Space Research (INPE), São José dos Campos, SP, Brazil.

^c Head of CBERS Applications Program, Earth Observation Coordination (OBT), National Institute for Space Research (INPE), São José dos Campos, SP, Brazil.

^d Remote Sensing Division, National Institute for Space Research (INPE), São José dos Campos, SP, Brazil.

^e Engineering Office of Research, Image Processing Laboratory, South Dakota State University, Brookings, SD, USA.

* Corresponding author.

E-mails: vitors@iastate.edu (Vitor S. Martins); joao.soares@inpe.br (João V. Soares); evlyn.novo@inpe.br (Evlyn M. L. M. Novo); claudio.barbosa@inpe.br (Claudio C. F. Barbosa); cibele.teixeirapinto@sdstate.edu (Cibele T. Pinto); jeferson@dpi.inpe.br (Jeferson S. Arcanjo); kaleita@iastate.edu (Amy Kaleita).

Abstract

A practical atmospheric correction algorithm, called Coupled Moderate Products for Atmospheric Correction (CMPAC), was developed and implemented for the Multispectral Camera (MUX) on-board the China-Brazil Earth Resources Satellite (CBERS-4). This algorithm uses a scene-based processing and sliding window technique to derive MUX surface reflectance (SR) at continental scale. Unlike other optical sensors, MUX instrument imposes constraints for atmospheric correction due to the absence of spectral bands for aerosol estimation from imagery itself. To overcome this limitation, the proposed algorithm performs a further processing of atmospheric products from Moderate Resolution Imaging Spectroradiometer (MODIS) and Visible Infrared Imaging Radiometer Suite (VIIRS) sensors as input parameters for radiative transfer calculations. The success of CMPAC algorithm was fully assessed and confirmed by comparison of MUX SR data with the Landsat-8 OLI Level-2 and Aerosol Robotic Network (AERONET)-derived SR products. The spectral adjustment was performed to compensate for the differences of relative spectral response between MUX and OLI sensors. The results show that MUX SR values are fairly similar to operational Landsat-8 SR products (mean difference < 0.0062, expressed in reflectance). There is a slight underestimation of MUX SR compared to OLI product (except the NIR band), but the error metrics are typically low and scattered points are around the line 1:1. These results suggest the potential of combining these datasets (MUX and OLI) for quantitative studies. Further, the robust agreement of MUX and AERONET-derived SR values emphasizes the quality of moderate atmospheric products as input parameters in this application, with root-mean-square deviation lower than 0.0047. These findings confirm that (i) CMPAC is a suitable tool for estimating surface reflectance of CBERS MUX data, and (ii) ancillary products support the application of atmospheric correction by filling the gap of atmospheric information. The uncertainties of atmospheric products, negligence of the bidirectional effects, and two aerosol models were also identified as a limitation. Finally, this study presents a framework basis for atmospheric correction of CBERS-4 MUX images. The utility of CBERS data comes from its use, and this new product enables the quantitative remote sensing for land monitoring and environmental assessment at 20 m spatial resolution.

Keywords: CBERS, surface reflectance, CMPAC, Landsat-8, MODIS, VIIRS.

1. Introduction

The China-Brazil Earth Resources Satellite (CBERS) is a cooperative Earth Observation program that provides multi-spectral data for assessing and monitoring natural resources (Fonseca et al., 2014). As part of its second generation, CBERS-4 spacecraft was launched on December 7, 2014, and the Multispectral Camera (MUX) is one of the instruments on-board this platform. The MUX is a pushbroom imaging spectrometer acquiring data in the visible and near-infrared (VNIR) wavelengths across 120 km swath width. Due to the 20 m spatial resolution and open data policy, the MUX instrument provides a valuable dataset for monitoring most landscape features such as forest, roads, water bodies, and urban area. In addition, recent radiometric calibration has shown that MUX quality is comparable to Landsat-8 OLI data for the common spectral bands (Pinto et al., 2016a), which represents a positive measure for this multi-spectral sensor. Despite the potential of CBERS-4 MUX instrument to provide a reliable data at continental-scale, few studies have used this multi-spectral data, and no operational products have been developed for quantitative applications based on the surface reflectance.

The atmospheric scattering and absorption of sunlight have a significant impact on the top-of-atmospheric (TOA) radiance measured by the space-borne sensors (Tanré et al., 1979; 1981; Antoine & Morel 1998; Lyapustin, 1999). The atmospheric correction procedures become a prerequisite for accessing the surface spectral properties in the quantitative analysis. Several studies have focused on the atmospheric correction techniques deriving the surface bidirectional reflectance factor (BRF), also known as surface reflectance (SR) (Liang et al., 1997; 2001; Vermote et al., 2002). For instance, Moderate Resolution Imaging Spectroradiometer (MODIS) land team has been leading historical efforts for global surface reflectance products (e.g. MOD09, MCD19A1) (Justice et al., 2002; Vermote and Kotchenova, 2008; Lyapustin et al., 2012). Similarly, Landsat Ecosystem Disturbance Adaptive Processing System (LEDAPS) for Landsat-7 ETM+ and Landsat Surface Reflectance Code (LaSRC) for Landsat-8 OLI were developed to provide medium spatial resolution products at the global scale (Masek et al., 2006; Vermote et al., 2016). Recently, European Space Association has also started distributing Level-2 atmospherically corrected

product for Sentinel-2 MSI using a semi-empirical Sen2Cor algorithm (Muller-Wilm et al., 2013). These examples demonstrate the continuous research efforts for accurate atmospheric correction procedures and the implementation of radiative transfer (RT) models in the operational algorithms (Doxani et al., 2018), such as Second Simulation of the Satellite Signal in the Solar Spectrum (6SV) (Vermote et al., 1997).

The high variability of atmospheric constituents including aerosol loading, water vapor, and total-ozone burden imposes a critical challenge for atmospheric correction (Kaufman et al., 1997a; Gao et al., 2009). Such knowledge of the atmospheric condition is required as input parameters for RT calculations during satellite overpass. While water vapor content and total ozone-burden are more spatially stable for short periods (Zelazowski et al., 2011), aerosols represent the largest source of uncertainty in the atmospheric correction due to large variety of sources and strong scattering in the VNIR range (Fraser and Kaufman, 1985). For instance, Martins et al. (2018) show that aerosol scattering in the blue wavelengths can increase the TOA reflectance from ~0.06 to 0.25 for standard vegetation spectrum during burning season. Several algorithms were developed for aerosol retrieval in the last decades (Remer et al., 2005; Levy et al., 2007; Kahn et al., 2009; Lyapustin et al., 2011). The Dark Target method is the most common pixel-based technique used to estimate the aerosol loading from satellite measurements (Kaufman et al., 1997b). In this method, the aerosol optical depth (AOD) is determined through an empirical relationship assumption between the reflectance at visible wavelengths (0.47 and 0.66 μm) and short-wave infrared (SWIR, 2.1 μm) over the dark land targets, such as dense vegetation or dark soils. This technique supports the decouple of aerosol and surface signals, and becomes a theoretical basis for aerosol retrievals in the atmospheric correction of MODIS and Landsat-8 OLI products (Vermote et al., 2002; 2016). However, when space-born sensors do not allow an internal aerosol retrieval from the imagery itself, such as MUX sensor, an alternative approach is required to implement the independent data sources for atmospheric correction.

The moderate resolution aerosol products from other missions have been applied for atmospheric correction of the target satellite images (Jiménez-Muñoz et al., 2010; Zelazowski et al., 2011; Hu et al., 2014; Wang et al., 2016; Martins et al., 2017a). For instance, Jiménez-Muñoz et al. (2010) evaluated four

atmospheric profiles sources for atmospheric correction of satellite sensors (CHRIS, ASTER and TM). The authors emphasized the value of these data sources when in-situ data are scarce or not available. Likewise, Ju et al. (2012) performed the Landsat-7 ETM+ atmospheric correction using MODIS atmospheric products across United States. Although these products are useful to characterize the atmospheric conditions, there are often missing data because of cloud cover or poor-quality retrievals. In these cases, the gap filling procedure is typically implemented by assuming a default value (e.g. 0.06 AOD, Claverie et al., 2015) or applying the geostatistical techniques, such as natural neighbor interpolation (Ju et al., 2012; Roy et al., 2014). While the geostatistical interpolation techniques are reliable for regions with regular sample grid around the targeted pixel, the interpolated values may be outside the range when there are extensive missing data over large areas. In this context, an alternative approach is the combination of multi-data sources, such as MODIS and VIIRS aerosol products, to increase the spatial coverage of observed values (instead of interpolated). The advantage of this approach is that the atmospheric products have been achieving successful retrievals with global validation, providing a potential means to overcome limitations of atmospheric characterization for each CBERS MUX scene.

This paper describes an atmospheric correction algorithm, called Coupled Moderate Products for Atmospheric Correction (CMPAC), developed to retrieve the CBERS-4 MUX surface reflectance product across South America. The algorithm applies the moderate atmospheric products from MODIS and Visible Infrared Imaging Radiometer Suite (VIIRS) as input parameters for the widely-used 6SV radiative transfer model. The evaluation of MUX SR was performed based on the near-simultaneous Landsat-8 OLI observations (616 match-ups) and AERONET-derived SR (64 match-ups). The results show that the proposed algorithm had a success to derive the MUX SR data, and these retrievals presented a near-similar quality to those of Landsat OLI. This research is part of efforts to increase the usage of CBERS-4 data.

2. Data and pre-processing

2.1. CBERS-4 MUX images

The CBERS-4 satellite operates in a so-called sun-synchronous orbit (778 km altitude), crossing the equator at approximately 10:30 a.m. local time. The MUX instrument on-board of the CBERS-4 satellite is a pushbroom imaging spectrometer acquiring data at four spectral bands: blue (485 nm), green (555 nm), red (660 nm) and NIR (830 nm). Figure 1 shows a relative spectral response (RSR) of CBERS-4 MUX and Landsat-8 OLI sensors. Due to the narrow $\pm 4.4^\circ$ field of view and repeat cycle of 26-day, each scene tile may be acquired a maximum of 14 times per year (contrast of 22 or 23 images for Landsat). The MUX Level-4 processing provides 8-bit quantization and co-registration at sub-pixel accuracy. Currently, the National Institute for Space Research (INPE) is responsible for free data distribution at catalog website (<http://www.dgi.inpe.br/catalogo>). In this study, CBERS-4 MUX data (616 images) were obtained in the INPE catalog between 2015 and 2016 across South America. The atmospheric correction of MUX Level-4 data was performed as described in Section 3. The TOA reflectance is calculated from the digital number (DN) values using Equation 1:

$$\rho_{\lambda_i}^{\text{TOA}} = \frac{\pi \cdot L_{\lambda_i}^{\text{TOA}} \cdot d^2}{E_{\lambda_i}^\circ \cdot \cos \theta_s} \quad (1)$$

Where

- $\rho_{\lambda_i}^{\text{TOA}}$ TOA reflectance at the spectral band (λ_i);
- $L_{\lambda_i}^{\text{TOA}}$ TOA radiance [$\text{W} \cdot \text{m}^{-2} \cdot \text{sr}^{-1} \cdot \mu\text{m}^{-1}$] calculated applying the linear expression ($\text{DN}_{\text{TOA}} * G_{\lambda_i}^{\text{L}}$);
- G^{L} band-specific rescaling gain factor from Pinto et al. (2016a);
- d astronomical earth-sun distance [AU];
- $E_{\lambda_i}^\circ$ mean solar exo-atmospheric irradiance [$\text{W} \cdot \text{m}^{-2} \cdot \text{sr}^{-1}$] (Table 1); and
- θ_s solar zenith angle [degrees].

The original metadata (.xml file) was adapted to follow the same structure of Landsat MTL metadata, including sun-view angles, sun-earth distance, standard filenames, and radiometric coefficients.

Table 1. Description of MUX spectral bands, scaling factor and exo-atmosphere solar irradiance. The Landsat-8 OLI spectral bands are also presented.

	Center wavelength [μm]	Band wavelength [μm]	G^L Radiance scaling factor [$\text{W}\cdot\text{m}^{-2}$]	E° Solar Irradiance ($\text{W}\cdot\text{m}^{-2}\cdot\mu\text{m}^{-1}$)	OLI wavelength [μm]
Blue (B5)	0.485	0.450 – 0.520	1.68 ± 0.05	1958 ± 35	0.452 – 0.512 (B2)
Green (B6)	0.555	0.520 – 0.590	1.62 ± 0.05	1852 ± 29	0.533 – 0.590 (B3)
Red (B7)	0.660	0.630 – 0.690	1.59 ± 0.05	1559 ± 18	0.636 – 0.673 (B4)
NIR (B8)	0.830	0.770 – 0.890	1.42 ± 0.05	1091 ± 11	0.851 – 0.879 (B5)

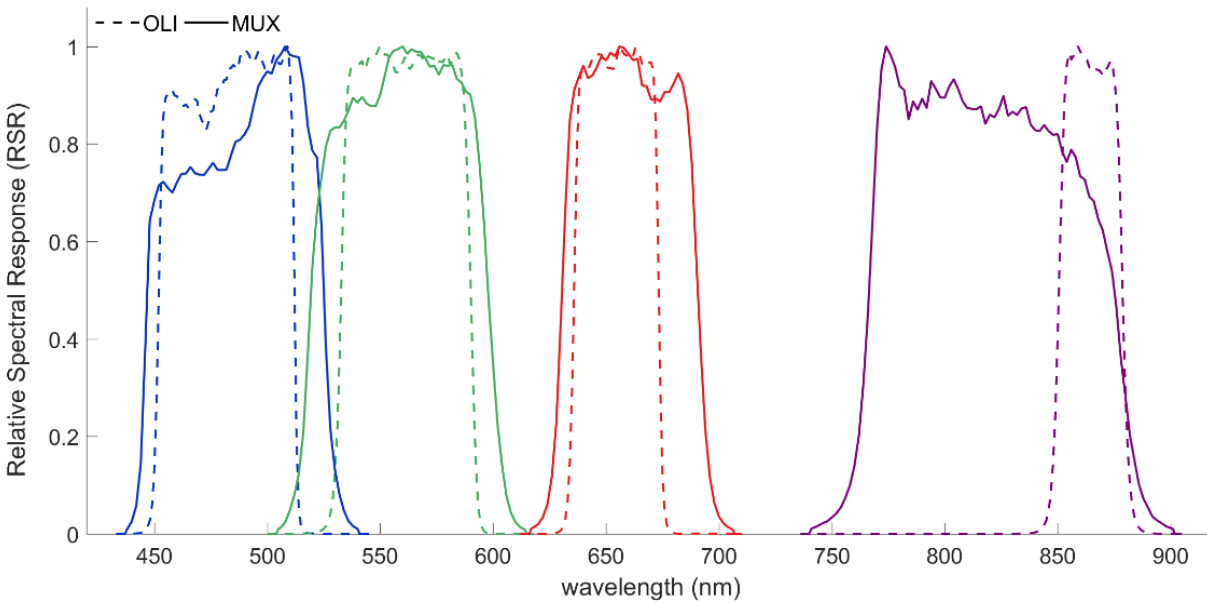


Figure 1. Relative spectral response of CBERS-4 MUX (solid line) and Landsat 8 OLI (dashed line) for the bands used in this study.

2.2. Moderate atmospheric products

2.2.1. MODIS C6 MAIAC product (MCD19A2)

The MODIS instruments were launched on board NASA Terra and Aqua satellites on February 2000 and June 2002, respectively (Justice et al., 2002). The Terra and Aqua platforms operate at sun-synchronous orbit, with crossing equator at ~10:30 am and ~1:30 pm local time, respectively. The MODIS sensor provides the near-daily observations, large swath width (~2330 km), 36 spectral bands (ranging from 0.415 to 14.5 μm) and three spatial resolutions (250, 500 and 1000 m according to bands). This unique

dataset allows the historical aerosol retrievals based on the Dark target and Deep Blue approaches (Remer et al., 2005; Hsu et al., 2013). Recently, a new advanced Multi-Angle Implementation Atmospheric Correction (MAIAC) algorithm was developed for MODIS measurements, providing a suite of atmospheric products at 1 km spatial resolution, such as AOD and columnar water vapor (CWV) (Lyapustin et al., 2011; 2012; 2018). The standard MODIS Collection 6 MAIAC product is a combined Terra/Aqua product (MCD19A2); this product offers a new dataset for the aerosol monitoring from regional to global scales.

In general, MAIAC algorithm implements a time-series analysis and multi-scale processing to retrieve the atmospheric products over dark and bright surface areas (Lyapustin et al., 2009). The main advantage of MAIAC is the prior knowledge of surface reflectance properties from multi-angle MODIS observations (up to 16 days), which minimizes the empirical assumptions applied in the standard MODIS products (Hilker et al., 2012). The MAIAC aerosol product is gridded into 1200 x 1200 km² standard MODIS tiles with 1 km sinusoidal grid, and the reference numbers of these tiles are presented in the Lyapustin et al. (2018). The algorithm uses this tiling scheme to allow the observation of the same 1 km grid over time, supporting the application of time series analysis. Previous evaluation of MAIAC aerosol showed that new product is suitable for fine spatial monitoring (Superczynski et al., 2017; Lyapustin et al., 2011). Recently, comprehensive validation of MAIAC retrievals was performed across South America (Martins et al., 2017b), and the results showed that more than 66% of MAIAC retrievals are falling within the expected error ($\pm 0.05 + 0.05 \times \text{AOD}$).

In this study, the standard MCD19A2 product derived from MAIAC algorithm was obtained from the Level-1 and Atmosphere Archive & Distribution System (LAADS) Distributed Active Archive Center (DAAC) (<https://ladsweb.modaps.eosdis.nasa.gov/>). The MCD19A2 product contains AOD₅₅₀ and CWV retrievals from MODIS-MAIAC Terra (hereafter MAIAC_T) and Aqua (hereafter MAIAC_A) data in the HDF-4 files. Note that although the MCD19A2 is called combined product, the users are able to extract the retrievals from MAIAC Terra and Aqua separately. The orbit information (e.g. "Orbit_time_stamp") supports the extraction of MAIAC_T and MAIAC_A retrievals from multi-dimensional array. The pre-

processing of MCD19A2 product includes the extraction of daily AOD and CWV records between 2015 and 2016 across South America. These daily atmospheric products are stored in a well-organized structure for easy and rapid access by our algorithm. Moreover, the monthly climatology of aerosol and water vapor was calculated using MAIAC_T data between 2000 and 2015 (<http://www.dpi.inpe.br/atmc/>). Figure 2 illustrates the spatial coverage of coupled moderate products (MAIAC_T, MAIAC_A, and VIIRS), including the MUX L4 scenes on August 22th 2015.

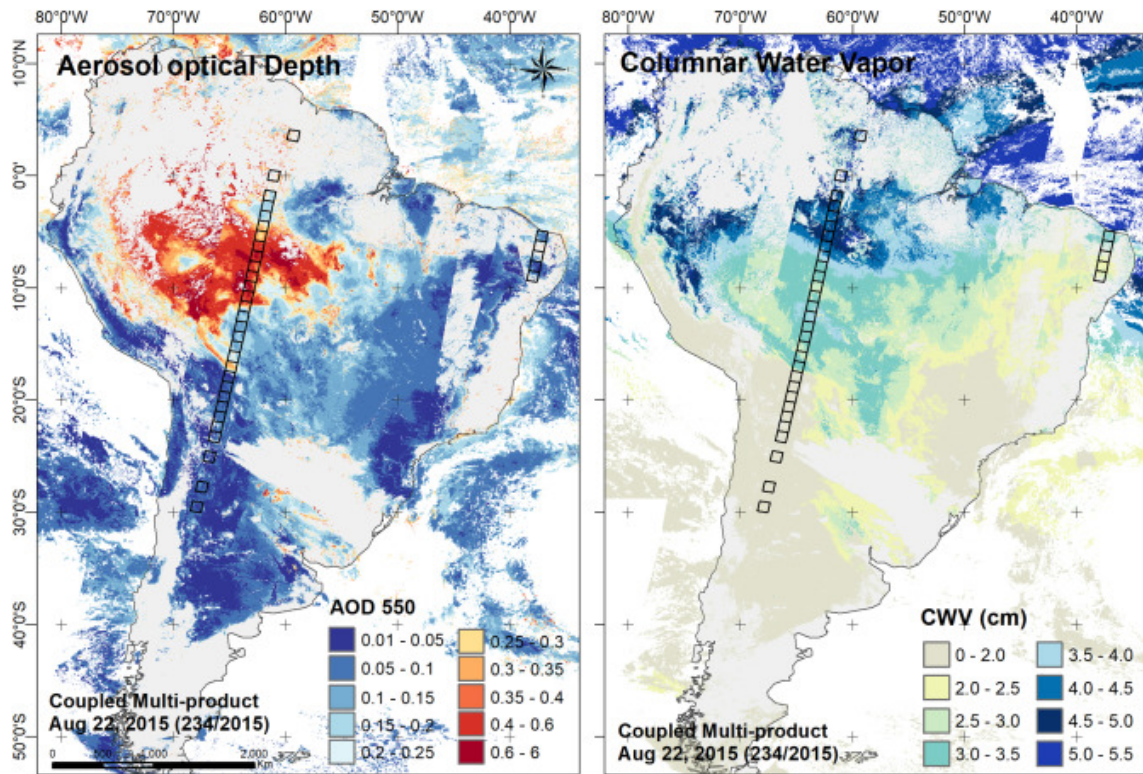


Figure 2. Coupled moderate atmospheric products for aerosol and water vapor at August 22th, 2015. The MUX Level-4 scenes illustrate the overlay of atmospheric products in this day.

2.2.2. MOD08 total ozone content

The Collection 6 level-3 MODIS products consist of several statistics derived from the Level 2 atmospheric products, such as aerosol (MOD04), water vapor (MOD05) and MOD07 atmospheric profiles (Hubanks et al., 2015). The MOD08 L3 provides atmospheric parameters such as total-zone burden, temperature, and moisture profiles with coarse spatial resolution ($1^\circ \times 1^\circ$) at the global scale. A detailed

description can be found in Seemann et al. (2003) and Algorithm Theoretical Basis Documents at https://modis.gsfc.nasa.gov/data/atbd/atmos_atbd.php. Here, the total-ozone burden was derived from daily MOD08-D3 Collection 6 products. A total of 731 global daily images were downloaded from the LAADS DAAC (<https://ladsweb.modaps.eosdis.nasa.gov/>) within 2015 - 2016 period. Furthermore, we computed a monthly climatology of total ozone over South America using the 15-year daily product (2000-2015). This later was calculated to support the gap filling procedures (Section 3.2). The seasonal gradient of total-ozone ranges from 200 to 360 DU across South America, with highest records in the September to November October at high latitudes. For further knowledge, the readers can find reference literature in Fioletov et al. (2008) and Ziemke et al. (2011).

2.2.3. VIIRS Aerosol EDR

The Visible Infrared Imaging Radiometer Suite (VIIRS) instrument was launched in October 2011 on-board the Suomi National Polar-Orbiting Partnership (S-NPP) satellite (Cao et al., 2014). The VIIRS S-NPP operates on a sun-synchronous orbit (824 km altitude) crossing the equator at 13:30 LT ascending node (similar to Aqua-MODIS). The VIIRS instrument delivers daily global observations with 22 spectral bands (0.412–12.05 μm) and becomes part of new generation of multi-disciplinary sensors. Based on its the heritage from MODIS, the VIIRS AOD Environmental Data Record (EDR) provides AOD level 2 products at 6 km spatial resolution (Jackson et al., 2013; Liu et al., 2014). The AOD retrievals are derived from 8 x 8-pixel aggregation of the Intermediated Product retrievals (750 m) for 11 wavelengths (412 – 2250 nm). The AOD records range from 0 to 2.0, and the retrievals have quality flags of unproduced (QF = 0), low (QF = 1), medium (QF = 2) and high (QF = 3) quality. Previous validation against Aerosol Robotic Network (AERONET) records have shown that more than 68% of VIIRS AOD retrievals fall within the EE ($\pm 0.05 \pm 0.15 \times \text{AOD}$) initially purposed for MODIS products (Liu et al., 2014). In this study, the VIIRS AOD EDR product (product ID: VAOOO) were download from National Oceanic and Atmospheric (NOAA) Comprehensive Large Array-data Stewardship System (CLASS) (www.class.noaa.gov). The daily VIIRS AOD data were obtained from 2015 to 2016 across South America. The pre-processing of

VIIRS AOD for each tile is described as follows: (i) extraction of AOD 550 from HDF file, (ii) conversion by scaling factors, (iii) filtering of high-quality AOD retrievals (QF=3) and (iv) mosaic of all daily tiles over South America. This pre-processed product is ancillary information in the atmospheric correction which is discussed in the next section.

3. Implementation of the CMPAC algorithm

The conceptual framework of this study is presented as a flowchart in Figure 3. The CMPAC algorithm was developed for atmospheric correction of CBERS-4 MUX using independent moderate atmospheric products, such as MODIS-MAIAC and VIIRS EDR.

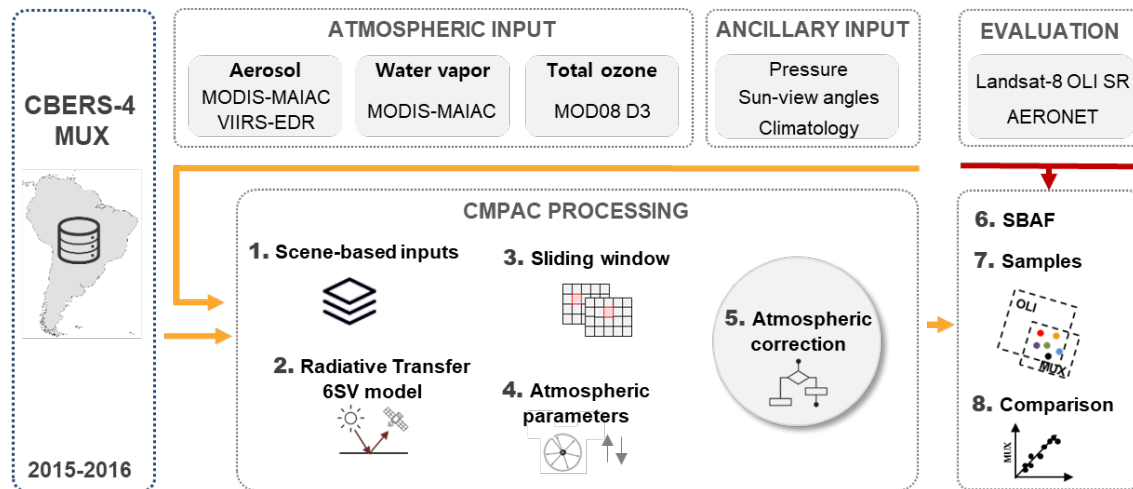


Figure 3. Flowchart for MUX surface reflectance retrievals and its evaluation.

3.1. Radiative transfer 6SV model

The 6SV is a robust RT code that provides a complete description of a physical-optical system for propagation of the solar radiation through the atmosphere (Vermote et al., 1997). This model comprises the radiation polarization, gaseous absorption, anisotropic or Lambertian surface, target's elevation and atmospheric scattering reflectance. Kotchenova et al. (2006) found a good performance of 6SV model compared to others RT codes, while it also shows satisfactory agreement relative to benchmark Breon's Monte Carlo code (<http://rtcodes.ltdri.org/>). Moreover, the 6SV code is the reference RT code to compute

the look-up tables for MODIS and VIIRS atmospheric correction. This RT model allows a straightforward calculation of both aerosol and Rayleigh scattering and atmospheric absorption due to ozone, uniformly mixed gases, and variable column water vapor. By assuming an isotropic and homogeneous surface, Equation 2 describes the TOA reflectance (ρ_{TOA}) and radiative transfer parameters (Tanré et al., 1979; Vermote et al., 1997):

$$\rho_{\text{TOA}}(\lambda_i) = T_{\text{og}}(\lambda_i, m, P) \left[\rho_{\text{R+A}}(\lambda_i, \theta_v, \theta_s, \varphi, P, \text{Aer}) + \frac{t^\downarrow(\lambda_i, \theta_s, P, \text{Aer}) \times t^\uparrow(\lambda_i, \theta_v, P, \text{Aer}) \times \rho_{\text{SR}}(\lambda_i)}{1 - S_{\text{R+A}}(\lambda_i, P, \text{Aer}) \times \rho_{\text{SR}}(\lambda_i)} \right] T_{\text{O}_3}(\lambda_i, m, U_{\text{O}_3}) \times T_{\text{H}_2\text{O}}(\lambda_i, m, U_{\text{H}_2\text{O}}) \quad (2)$$

Where

- T_{og} gaseous transmittance of the major absorbing gases (CO_2 , CH_4 , NO_2 , and others);
- T_{O_3} ozone (O_3) transmittance due to total ozone content (U_{O_3});
- $T_{\text{H}_2\text{O}}$ water (H_2O) transmittance due to total water content ($U_{\text{H}_2\text{O}}$);
- $\rho_{\text{R+A}}$ atmospheric intrinsic reflectance due to Rayleigh and aerosol scattering;
- Aer aerosol optical properties including aerosol single-scattering albedo (ω_0), aerosol scattering phase function ($P_a(\Theta)$), and aerosol loading at 550 nm (AOD);
- m geometrical air mass factor is computed by $m = (\mu_s^{-1} + \mu_v^{-1})$, $\mu_s = \cos \theta_s$ and $\mu_v = \cos \theta_v$;
- t^\downarrow or t^\uparrow atmospheric transmittance from the sun to target (downward) and target to the sensor (upward), respectively;
- $S_{\text{R+A}}$ atmosphere spherical albedo to account for multiple surface-atmosphere reflections;
- P atmospheric pressure derived from altitude;
- θ_v view zenith angle;
- θ_s solar zenith angle; and
- φ relative azimuth angle is the solar azimuth angle (φ_s) minus view azimuth angle (φ_v), $\varphi = \varphi_s - \varphi_v$.

Solving the equation for surface reflectance (ρ_{SR}):

$$\rho_{\text{SR}} = (\rho_{\text{TOA}}/T_g - \rho_{\text{R+A}}) / [t^\downarrow(\theta_s) t^\uparrow(\theta_v) + S_{\text{R+A}}(\rho_{\text{TOA}}/T_g - \rho_{\text{R+A}})] \quad (3)$$

These transfer parameters are computed by each run in the 6SV model, and then, the surface reflectance is derived from TOA reflectance using Equation 3. Note that we neglected the interaction term between gaseous absorption and the aerosol and molecular scattering, which is treated independently. The negligence of this interaction might introduce minor bias in the $\rho_{\text{R+A}}$ term where both strong absorption

and scattering regimes occur concurrently, such as MUX NIR. The spectral response function of MUX was incorporated into the 6SV running code.

3.2. Model input data, boundary condition, and model output

In this section, we describe the input data (Section 2.2) and the implementation of CMPAC algorithm. This algorithm was originally developed to use the multiple sources of atmospheric data as primary input for radiative transfer 6SV model. The current version relies upon pre-processing of (i) AOD 550 nm from MAIAC and VIIRS retrievals; (ii) water vapor content from MAIAC retrievals; (iii) Total-ozone burden from MOD08 product; (iv) surface elevation from Shuttle Radar Topography Mission (SRTM) void-filled data; and (v) calculation of solar and view geometries at 20 km grid spacing. Prior knowledge of atmospheric condition is required for RT applications, and to do so, the routine processing is divided into three modules: (i) pre-processing of moderate atmospheric products; (ii) generation of the the input 6SV parameters for each scene; (iii) application of the sliding window technique for atmospheric correction. When CMPAC runs for a specific image, the algorithm creates scene-based input data to compute the radiative transfer parameters. In this stage, an elementary processing area was defined as 20 x 20 km for sliding window algorithm; this is a practical procedure to assure that all pixels have valid record assuming spatial homogeneity of atmospheric constituents ($\sim 30 - 40 \text{ km}^2$) (Anderson et al., 2003).

The MAIAC_T products were used as a primary source of AOD and water vapor, while ozone content is obtained from the MOD08-D3 product (also Terra platform). The rationale for MAIAC_T is a near-time overpass between Terra and CBERS-4 (few minutes apart). Despite large coverage and daily retrievals of MAIAC_T, the cloud cover or poor-quality retrievals are often expected, and a gap-fill procedure using MAIAC_A was developed to account for missing values. When both MAIAC_T and MAIAC_A retrievals have failed, VIIRS AOD retrievals then are used as the third option for spatially filling missing values. More specifically, an iterative scheme was adopted to fill the atmospheric input data by following the sequential priority logic: MAIAC_T \rightarrow MAIAC_A \rightarrow VIIRS \rightarrow monthly climatology. Fortunately, we observed that vast majority of cloud-free MUX images are followed by valid MAIAC_T retrievals due to

near-similar time overpass between these platforms, as one should expect. The two candidates for aerosol models are “continental” and “biomass burning”; the selection of model relies on global aerosol mixture from Taylor et al. (2015) at image time and geographic location. These aerosol models comprise a large proportion of cases over land (Masek et al., 2006). The surface elevation was derived from SRTM 3 arc-second (90 meters). In summary, the following steps are the basic processing for MUX atmospheric correction:

- 1) Extract the metadata from the MUX image;
- 2) Convert from DN to TOA reflectance;
- 3) Compute the solar and view angles, select the aerosol model and acquire surface elevation;
- 4) Build-in the input parameters from pre-processing moderate atmospheric products;
- 5) Run the 6SV code deriving the atmospheric transfer parameters; and
- 6) Convert to surface reflectance in the sliding window technique.

Lastly, CMPAC processor generates the MUX spectral bands at SR level, updating the new metadata with scene parameters. The atmospheric correction procedure is applied to all pixels over land.

3.3. Evaluation: cross-comparison with Landsat-8 OLI and AERONET-derived SR

The evaluation of MUX SR values was performed by comparing to (i) Landsat-8 OLI SR Level-2 product and (ii) AERONET-derived SR. Ideally, this evaluation should be performed using in-situ radiometric measurements, but there are no systematic measurements at spatial and temporal scale for this validation. As many others, we adopted the cross-comparison of two satellite products. The Landsat-8 and CBERS-4 satellites operate in sun-synchronous orbits and have small difference of crossing time at the equator. In additional, MUX and OLI sensors have near-similar VNIR bands, allowing this comparison for common spectral bands. To do so, the cross-comparison of MUX and OLI surface reflectance was performed using 616 image pairs (Figure 4). Note that OLI footprint (~185 km) might intersect more than one MUX scene (~120 km) at the same day. The Landsat-8 OLI Level-2 surface reflectance was delivered by ESPA on-demand system (<https://espa.cr.usgs.gov/>), and we used only four VNIR bands: 0.482 μm

(B2), 0.561 μm (B3), 0.655 μm (B4), and 0.865 μm (B5). This evaluation approach is rather straightforward: random points (500 to 1000) are distributed across overlapping area of the image pair, and a mean reflectance value of 3 x 3-pixel window around these points is calculated for each spectral band. It should be mentioned that visual inspection was performed to exclude those points affected by cloud or cloud shadow, but we are still expecting some noisy points due to cloud contamination. Given the difference of relative spectral responses (RSR) between MUX and OLI bands (Fig. 1), spectral band adjustment factors were estimated to reduce this intrinsic source of divergence – this is a vital step for multi-sensor exercise. A detailed description is presented in Appendix A, and the adjustment factors were applied to MUX SR values before any comparison with OLI SR values (Table A2).

The evaluation of MUX SR against the AERONET-derived SR product was also performed. The AERONET is a global sun-photometer network to monitor the aerosol optical properties. These sun-photometer data allow computing the aerosol optical depth from 340 to 1020 nm range, while the water vapor is calculated in the absorption band around 940 nm. The AERONET dataset is considered the ground-truth reference for aerosol retrievals, and many studies have used these data for validation of satellite-derived RS products (Wang et al., 2009; Franch et al., 2014; Claverie et al., 2015). In this practice, atmospheric correction of MUX image was performed using the AERONET L2 records as input parameter for 6SV model, hereafter $\text{MUX}_{\text{AERONET}}$. According to data availability, 11 AERONET sites were selected within 2015-2016, ranging from Amazon rainforest to cropland areas in the central-west (Figure 4). The AERONET data were used for atmospheric correction of spatial subsets (10 x 10 pixels) centered on each site. The averaged AERONET measurements within ± 30 min of CBERS overpass was used in this exercise. Since AERONET sun-photometer does not record AOD at 550 nm, data were interpolated to 550 nm using Ångström empirical expression (Eck, 1999). It is important to highlight that the only difference between CMPAC retrievals and AERONET-derived SR was the input AOD and CWV values.

The results were assessed by statistical metrics, such as Root-Mean-Square Deviation (RMSD), mean difference (BIAS), and relative error (RE) between MUX SR and reference data (Landsat or AERONET-derived) as follows:

$$\text{RMSD} = \sqrt{\frac{\sum_{i=1}^N (\text{SR}_{\text{MUX}}(\lambda) - \text{SR}_{\text{REF}}(\lambda))^2}{N}} \quad (4)$$

$$\text{BIAS} = \frac{1}{N} \sum_{i=1}^N \text{SR}_{\text{MUX}}(\lambda) - \text{SR}_{\text{REF}}(\lambda) \quad (5)$$

$$\text{RE} = \left(\frac{1}{N} \sum_{i=1}^N \frac{|\text{SR}_{\text{MUX}}(\lambda) - \text{SR}_{\text{REF}}(\lambda)|}{\text{SR}_{\text{REF}}(\lambda)} \right) \times 100 \quad (6)$$

Where SR_{MUX} is the MUX surface reflectance at the spectral band (λ); SR_{REF} is the surface reflectance from Landsat-8 OLI or AERONET-derived SR estimates; N is the number of observations.

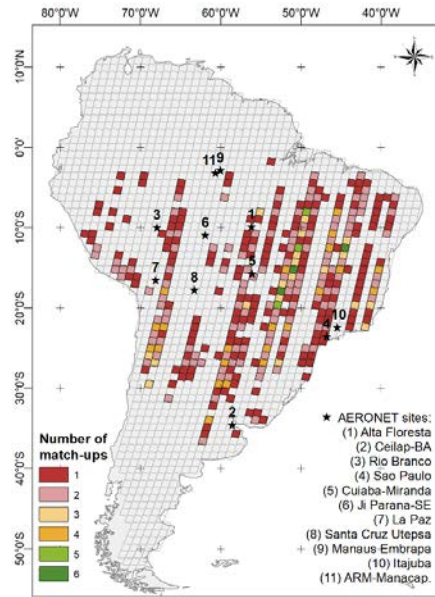


Figure 4. Spatial distribution of the number of selected images used in the inter-comparison MUX and OLI surface reflectance within 2015-2016 period. The AERONET sites are shown in the bottom-right list.

4. Results

Figure 5 shows the comparison of MUX surface reflectance derived from CMPAC (y-axis) and AERONET-based (x-axis) measurements. Again, the only difference between these datasets is the input parameter for aerosol and water vapor content. A high correlation was found between $\text{MUX}_{\text{CMPAC}}$ and

$\rho_{\text{MUX}_{\text{AERONET}}}$ for all spectral bands, with a correlation coefficient (R) close to unity and mean difference lower than 0.002. Since AERONET data are recognized as most reliable aerosol optical measurement, the AERONET-derived SR is the truth reference used in several studies for satellite evaluation (Ju et al., 2012; Claverie et al., 2015). The high agreement of CMPAC and AERONET SR is a positive measure for our study because it confirms that the input parameters (mostly MAIAC_T) are suitable to characterize the atmospheric conditions. However, these high-quality measurements are scarce over South America and only represent the local aerosol context. Then, subsequently, the cross-comparison of MUX and OLI SR values provides further assessment of CBERS MUX retrievals across several surface targets and under atmospheric conditions.

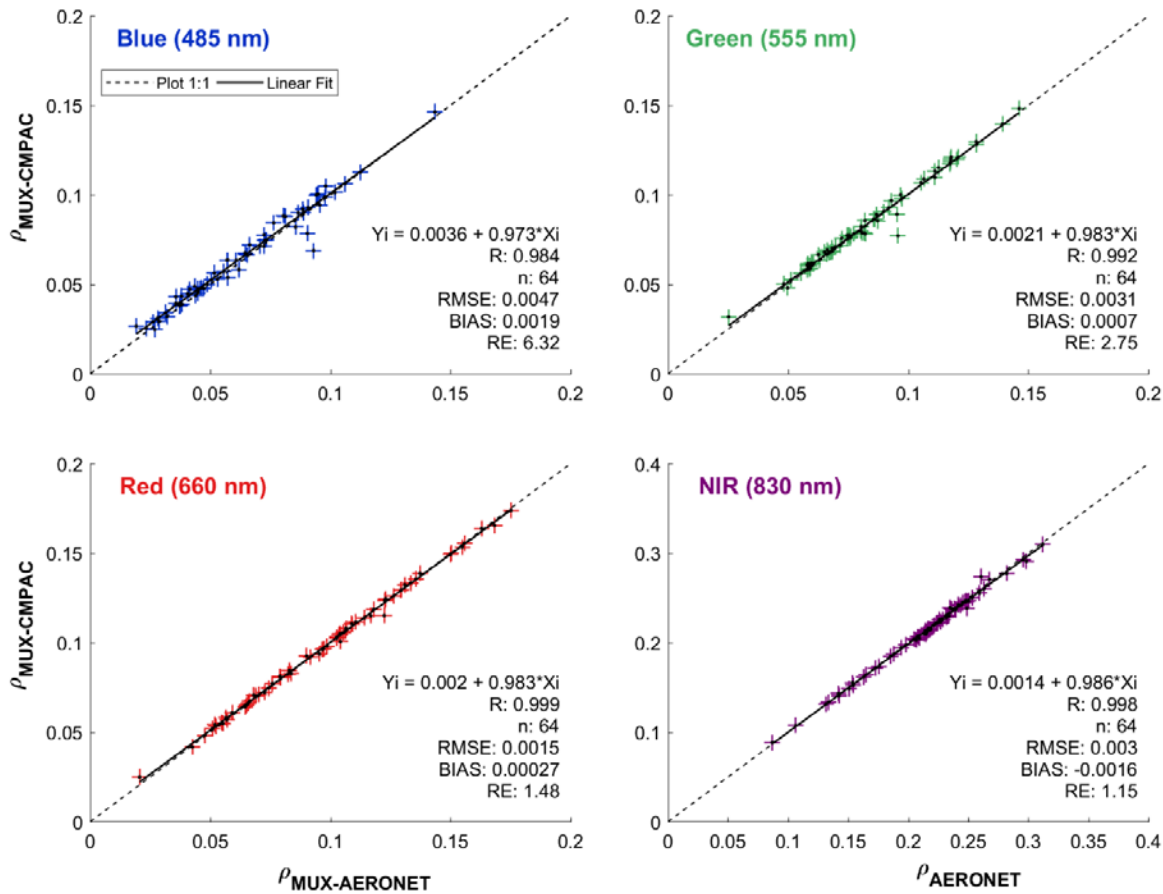


Figure 5. Scatter plots of MUX (y-axis) and AERONET-derived (x-axis) surface reflectance data for all spectral bands. The AERONET-derived SR, or reflectance truth, is obtained by correcting the TOA reflectance of MUX using AERONET as input for aerosol and water vapor. The statistical metrics are linear regression equation, correlation coefficient (R), number of samples (n), root-mean-square-deviation (RMSD), mean difference (BIAS), and relative error (RE).

Figure 6 shows the number of coincident MUX and OLI images per month. We observed that the most coincident images are acquired during the dry season due to the typical low cloud cover in this period (June to October). Moreover, the dataset includes at least nine image-pairs from each month, which is suggestive for a wide range of atmospheric conditions in this comparison exercise. Figure 7 illustrates the visual contrast between true color composite from MUX DN and SR at September 28, 2017 (path 162 and row 131). This example gives a visual perception about the benefits of radiometric conversion from ND_{TOA} to surface reflectance, such as the contrast between land surface features.

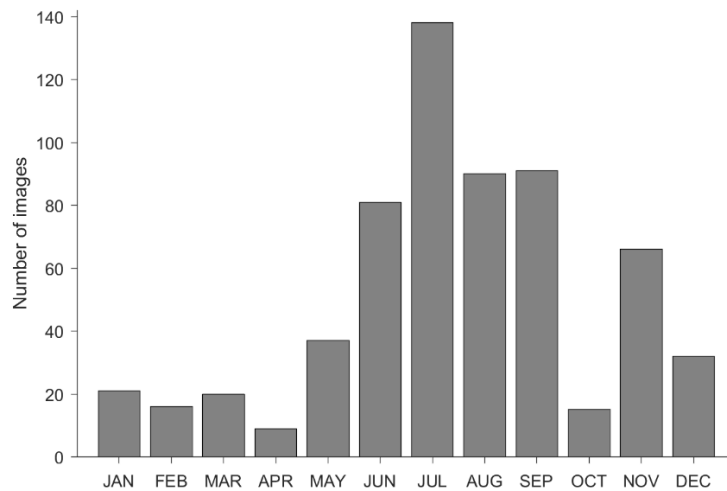


Figure 6. The number of coincident MUX and OLI images used in this study (2015-2016).

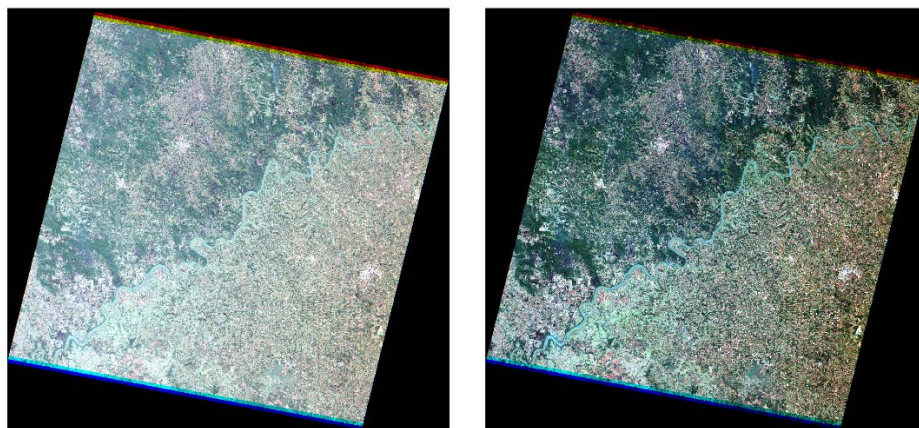


Figure 7. True color composite of the MUX bands using raw digital number (left) and surface reflectance (right) at September 28, 2016. These images are displayed with the same stretch for RGB bands (no contrast or histogram handle).

Figure 8 shows the comparison of CBERS-4 MUX and Landsat-8 OLI surface reflectance within the 2015-2016 period. The data points were randomly derived from 616 image-pairs, and spectral band adjustment was applied to MUX SR before this comparison (see Appendix A). These sampling points include a large variety of surface targets and atmospheric conditions, from the Atacama Desert to dense Amazon rainforest (Figure 4). The overall results showed a fair correlation between MUX and OLI SR products, with R close to unity ($R > 0.92$) and small mean difference (bias < 0.0062 , reflectance unit) for all spectral bands (Table 2). Furthermore, the scatter points are mostly close to 1:1 line and the slope of linear regression between MUX and OLI ranges from 0.887 to 0.981. The relative error reduces from blue (22%) to NIR (7.7%) band; this is expected due to stronger atmospheric scattering at short wavelengths. However, the mean difference at the blue band is lower (-0.0032) than other bands (eg.: NIR is 0.0062). Note that relative error is high for very low SR values, and the most SR values in the blue spectral band are lower 0.1; on the other hand, NIR reflectance values are typically higher than 0.2.

The comparison between MUX and OLI showed a slight underestimation for blue, green and red spectral bands; the boxplot of mean difference clearly reveals the negative bias. Note that Landsat-8 OLI SR implements an internal aerosol algorithm, relying on the dark targets for accurate aerosol retrievals. Therefore, while the Landsat product is used as “reference” in this study, this dataset has its own uncertainties and this cross-comparison evaluation provides a relative error metrics instead absolute error. Moreover, others factors might affect this evaluation such as calibration issues, residual cloud contamination, and negligence of bidirectional effects. Even under these circumstances, however, these findings show the potential of CMPAC processor to retrieve the MUX surface reflectance, with good agreement between these products.

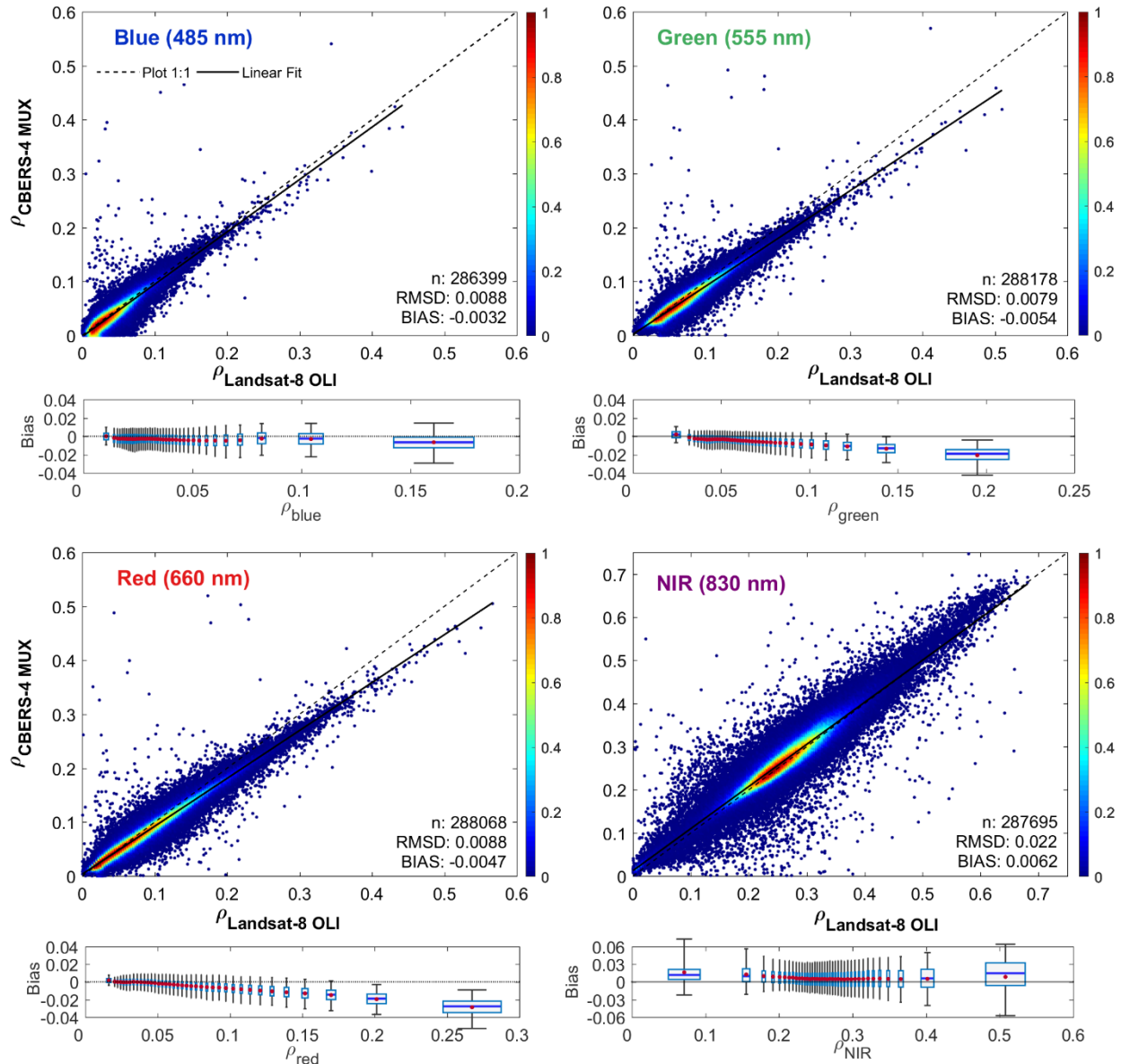


Figure 8. Scatter plots of MUX (y-axis) and OLI (x-axis) surface reflectance data for all bands. The statistical metrics are described in the right-bottom text as follows: number of samples (n), root-mean-square-deviation (RMSD), and mean difference (BIAS). The boxplots show mean difference between MUX and OLI (y-axis) as a function of surface reflectance (x-axis). The box edge represents 25 and 75%; whiskers are 5 – 95%; and the central line (blue color) and dot (red color) are median and mean, respectively.

Table 2. Statistical metrics of cross-comparison between MUX and OLI surface reflectance data presented in Figure 8. The variables are the correlation coefficient (R), the root-mean-square-deviation (Eq. 4), the mean difference (Eq. 5) and the relative error (Eq. 6).

MUX bands	Linear regression	R	Root mean square deviation (reflectance)	Bias or Mean difference (reflectance)	Relative error (%)
Blue (485 nm)	$\rho_{MUX} = -0.0021 + 0.970 \times \rho_{OLI}$	0.923	0.0088	-0.0032	22.0
Green (555 nm)	$\rho_{MUX} = 0.0021 + 0.887 \times \rho_{OLI}$	0.956	0.0079	-0.0054	11.4
Red (660 nm)	$\rho_{MUX} = 0.0036 + 0.888 \times \rho_{OLI}$	0.979	0.0088	-0.0047	11.5
NIR (830 nm)	$\rho_{MUX} = 0.0130 + 0.981 \times \rho_{OLI}$	0.946	0.022	+0.0062	7.7

Figure 9 illustrates the MUX and OLI SR values from the red band (0.66 μm) and the histogram plots for each VNIR band on August 9 2015. The visual inspection shows that both MUX and OLI red bands are fairly similar; land targets are clearly identified across both images. The radiometric resolution of MUX (8-bit) and OLI (12-bit) generates a slight contrast in the gradient of reflectance values, while the 20 m spatial resolution of CBERS (versus 30 m Landsat) provides more details for small land features. While this inspection gives the qualitative assessments for these images (red), the histogram distributions of surface reflectance show near-identical shape and magnitude for all spectral bands. The mean absolute difference between MUX and OLI was lower than -0.006. It should be noted that spectral band adjustment procedure is a vital step, especially for NIR band which the difference of RSR reaches up to 25 % for surface targets with high NDVI.

A time series analysis using remotely sensed imagery requires atmospherically corrected data. Figure 10 presents the temporal analysis of normalized difference vegetation index (NDVI) from agricultural pixels in Central Brazil (Lat.: -15.32, Lon.: -45.70). We observed that integrated MUX and OLI data were able to represent this single-crop cycle from 2015 and 2016. The seasonal variability of NDVI is consistent with crop growth (plant cycle and harvesting), with maximum records in the peak summer and the minimum records during winter. The combination of MUX and OLI observations overcomes the cloud obstacles, increasing the number of clear-sky images over the study area. Since the multi-sensor data integration is a relevant topic for time-series analysis of land change, these results suggest the potential of MUX SR values in this application.

CBERS-4 MUX 2015-08-09 (162/127)

Landsat-8 OLI 2015-08-09 (224/077)

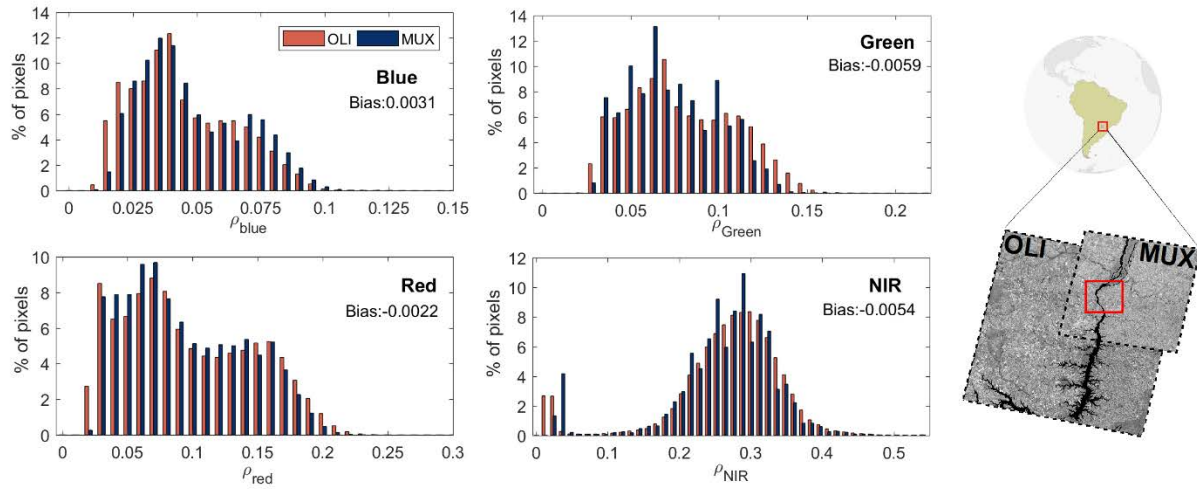
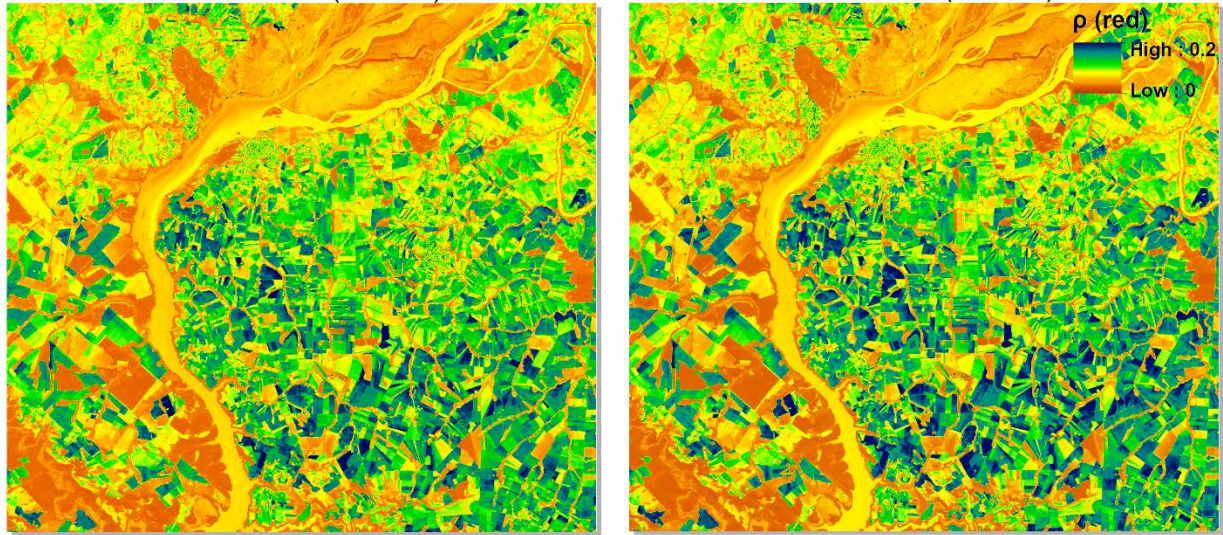


Figure 9. Example of MUX and OLI surface reflectance acquired on August 9 2015. The histogram distribution of surface reflectance shows similarities between sensor products.

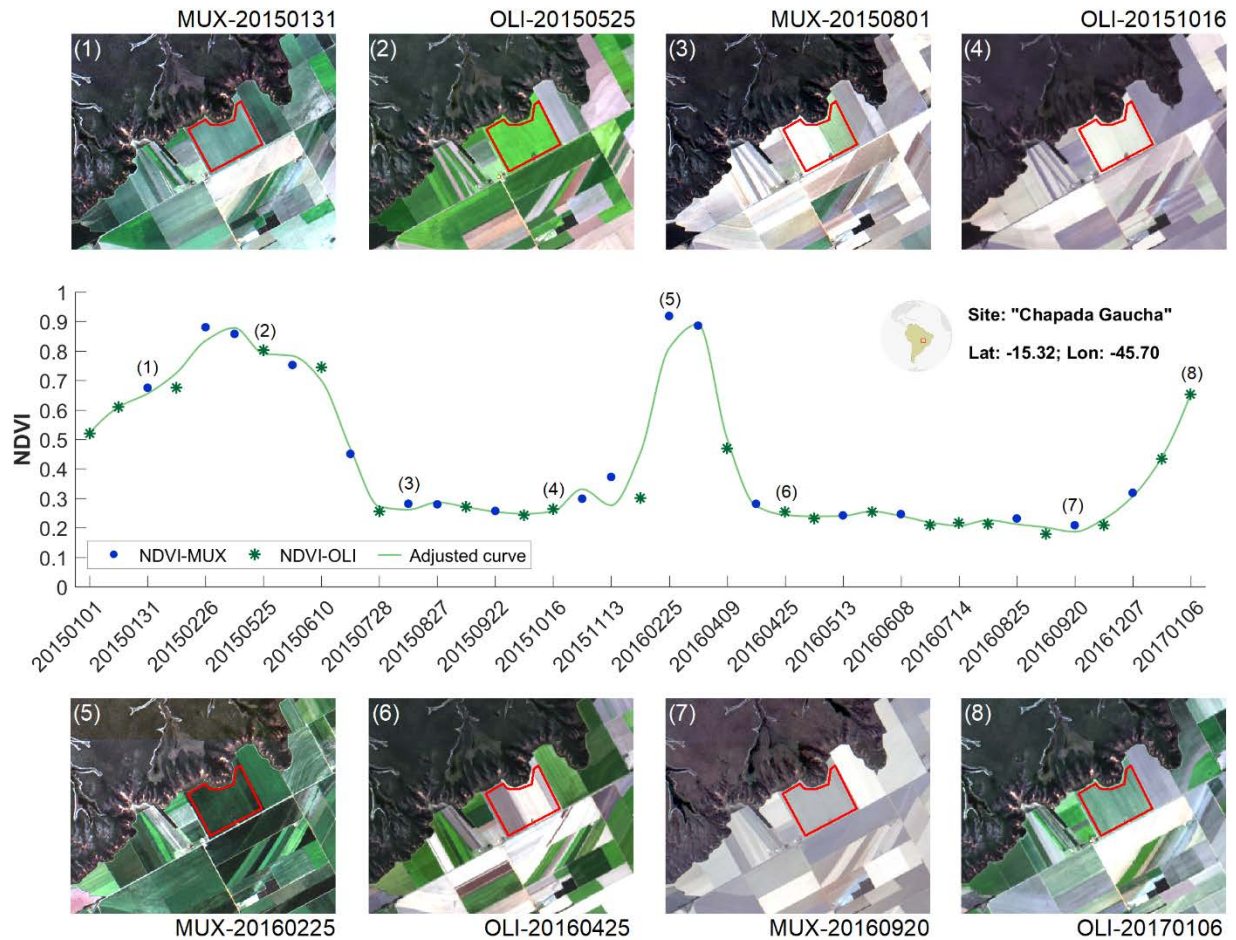


Figure 10. Time series NDVI profile coupling MUX and OLI SR data at Central-West region, Brazil. This result is shown the potential application of integrated data. Note that x-axis is irregular in chronological time, and the adjusted curve was obtained from Savitzky–Golay filter.

5. Discussion

The CBERS-4 MUX archive is a valuable resource for scientific studies at continental-scale, but no quantitatively reliable product was previously proposed for this multi-spectral data. In this study, we introduced an atmospheric correction algorithm, called CMPAC, to retrieve the CBERS-4 MUX surface reflectance product. The CMPAC is a modular algorithm with distinct components for operational application, including the pre-processing of ancillary atmospheric products and implementation of transfer coefficients in the sliding window technique. The performance of this algorithm was assessed by comparing MUX SR with Landsat-8 products and AERONET-based SR values. The results shown in Figs 5 and 8

confirm that the MUX SR values are consistent and near-similar to those values derived from Landsat-8 OLI and AERONET-based SR. The large number of pair-points are around the 1:1 line and mean difference is lower than 0.0067 (expressed in reflectance). While AERONET data allow the atmospheric correction using the highest quality of aerosol measurements, the evaluation was limited to few match-ups (64) and local aerosol conditions. In this context, the cross-comparison between MUX and OLI SR products becomes a practical alternative for an extensive assessment. A total of 616 image-pairs (and more than 286,000 random points) were used for this evaluation across South America. The high agreement of MUX and OLI SR products is an important result of this study (Table 2) and underline the potential of combining these datasets for quantitative studies. These findings also confirm that (i) CMPAC is a suitable tool for estimating surface reflectance and (ii) ancillary products provide spatially explicit information to represent the atmospheric conditions over each scene.

The results of this study are within the range of previous findings for atmospheric correction approaches (Vicente-Serrano 2008; Maier-Sperger et al., 2013; Feng et al., 2013; Vuolo et al., 2015; Claverie et al., 2015; Zhang et al., 2018) and MODIS atmospheric products have been applied in several studies related to atmospheric correction. For instance, Ju et al. (2012) evaluated the Landsat-7 ETM+ SR derived from LEDAPS and MODIS-based atmospheric correction methods over the United States. The authors found that the accuracy of MODIS-based Landsat SR was higher than LEDAPS (except the green band), with a mean difference between 0.001 and 0.006, and slope of linear regression ranging from 0.952 to 1.05. Similarly, Roy et al. (2014a) implemented the MODIS-based Landsat atmospheric correction algorithm into the NASA Web-enabled Landsat Data (WELD) project. The authors recognized that the MODIS-based approach is reliable in most cases – although it might introduce some uncertainties during biomass burning or dust storm events. Additionally, Vermote et al. (2016) performed a relative assessment of Landsat-8 OLI comparing with MODIS Aqua surface reflectance, and they found the mean absolute difference between 0.001 and 0.009. Note that the standard Landsat-8 SR product applies ancillary products for water vapor and ozone, while the aerosol retrievals are derived from the image itself (Kaufman et al., 1997b). Since Landsat program has the long-term scientific efforts for the radiometric calibration and assessment of SR

products (Roy et al., 2014b), the agreement of MUX and OLI products is a positive measure to endorse the value of this MUX SR product.

The utility of satellite data comes from its use, and surface reflectance products can substantially increase the applications in the quantitative remote sensing. For instance, we illustrated the NDVI crop dynamic as support for land monitoring using the integrated MUX and OLI data (Fig. 10). In terms of methodology, the processing strategy for the MUX data was undertaken in the previous MODIS-based atmospheric correction algorithms (Hu et al., 2014; Roy et al., 2014a; Ju et al., 2012; Jimenez et al., 2010). Since the main dependence of these approaches is the ancillary atmospheric products, the performance of this approach is explained, at least in part, by the quality of the input parameters, such as MAIAC aerosol retrievals. In this sense, Martins et al. (2017b) performed the comprehensive assessment of MAIAC AOD retrievals across South America and found a high agreement between this satellite product and AERONET AOD measurements. The authors also show that the quality of MAIAC retrievals varies according to the land surface type (better performance in the dense vegetation than that of bright surfaces). Therefore, it is plausible that the errors of aerosol retrievals might influence the MUX surface reflectance in some regions, such as urban or arid-areas. Although it implies in some drawbacks, this novel product has been used for aerosol characterization across several regions, consolidating the application at fine 1 km resolution (Superczynski et al., 2017; Liang et al., 2018; Martins et al., 2018). In the same context, another source of uncertainty is the diurnal variation of aerosol during biomass burning season, but it is only a concern when the filling gap procedure using MAIAC_A or VIIRS-EDR AOD is applied instead of primary source (MAIAC_T). A further assumption made in this analysis is the statement that the MODIS and VIIRS products have near-similar quality retrievals (Liu et al., 2014), but there are regional biases due to the differences of aerosol algorithms and sensor characteristics (Levy et al., 2015; Superczynski et al., 2017). Consequently, the suggestion for users is to evaluate the pixel quality information for their applications.

Recently, many efforts have been made by INPE to increase the use of remote sensing across South America: a new catalog was released for data distribution allowing an easy search/download of CBERS data (<http://www.dgi.inpe.br/catalogo>). As part of these efforts, this research will contribute significantly

for the development of MUX SR product, but it is also opportune to remark that there are other opportunities with optical and thermal sensors on-board CBERS spacecraft (e.g. WFI, IRS, Panchromatic). Undeniably, CBERS-4 continues the legacy of the long-term binational program by providing technological advances since the CBERS-2B. For instance, the Wide-Field Imaging (WFI) camera provides a revisit time of 5 days, large swath width (866 km) and four VNIR bands at 64 m resolution (instead of two bands and 260 m resolution in the CBERS-2B). Despite the ongoing improvements in the CMPAC processor, the atmospheric correction of MUX images is now possible using the proposed algorithm, and it seems the right time for standard processing in the CBERS data. In addition, we emphasize that periodic calibration activities are highly recommended to maintain the standard quality of CBERS data, because the radiometric coefficients might change over time affecting the surface reflectance product.

6. Conclusion and future directions

In this study, a CMPAC processor was developed for the atmospheric correction of CBERS-4 MUX L4 data across South America. The large data volume and an insufficient number of spectral bands for atmospheric retrievals are challenges in the operational atmospheric correction routines for MUX data. The algorithm applies the ancillary MODIS and VIIRS atmospheric product in the 6SV radiative transfer code to derive the MUX surface reflectance. The assessment was performed by comparison of MUX SR with Landsat-8 OLI (616 match-ups) and AERONET-based SR (64 match-ups). The results showed that MUX SR is comparable with these datasets; the scatter points are close to 1:1 line and R is higher than 0.92. Despite slight underestimation of MUX relative to OLI SR, the mean difference was lower than 0.0062 (expressed in reflectance units) and these error metrics are comparable with previous studies for Landsat surface reflectance.

This purposed algorithm requires pre-processing of moderate atmospheric products, which might limit the real-time product at this stage. Since Terra platform is few minutes apart of CBERS overpass, the MAIAC_T product represents well the atmospheric condition for the CBERS overpass. The gap-filling procedure might introduce a certain level of uncertainty caused by diurnal variation of an aerosol condition,

especially, during burning season. Looking ahead, the next objective of this research is the implementation of routines in an operational mode, improving the time processing by creating look-up tables and defining the quality assurance (QA) band for each scene. Finally, CMPAC processor is a promising approach for MUX surface product and this study contributes to quantitative applications in the land monitoring and environmental assessment at spatial 20 m resolution.

Acknowledge

We gratefully acknowledge the Image Generation Division (DGI), as part of Earth Observation Coordination (OBT), for providing the MUX L4 data used in this study. We thank the USGS ESPA On-Demand System (<http://espa.cr.usgs.gov/>) for processing the Landsat surface reflectance products. We thank analysts and scientists at MODIS and VIIRS team for providing the freely available datasets. MAIAC products are available at <ftp://dataportal.nccs.nasa.gov/DataRelease/SouthAmerica/>. We thank the AERONET PI and their staff for the establishment and maintenance of the South America sites. The authors would like to thank Dr. Robin Wilson for providing Py6S (Python interface to 6SV) with full description (Wilson, 2013). The processed data and products in this study are available from the corresponding author upon reasonable request.

Appendix A

The relative spectral response (RSR) functions of MUX and OLI sensors are slightly different between spectral bands (Fig. 1). For instance, OLI has a relatively narrow NIR band (851 – 879 nm) avoiding the water vapor absorption (~840 nm), while the MUX NIR has a wide NIR range (770 – 890 nm). The comparison of these sensors requires a proper spectral adjustment to minimize the effects of RSR differences. Several studies pointed out the importance of adjustment factors for the cross-comparison of satellite sensors (Steve et al., 2003; Mishra et al., 2014; Claverie et al., 2015; Pinto et al., 2016b). Chander et al. (2013) evaluated the RSR differences of ETM+ and MODIS using spectral band adjustment factors (SBAF). The authors calculated the SBAF applying EO-1 Hyperion TOA reflectance (108 images) over the Libya 4 test site. While the pseudo-invariant targets (e.g. desert Libya-4) benefit the calculation of

SBAF values, the spectral adjustment is more complex for large number of land targets. For instance, Claverie et al. (2015) proposed a machine learning approach using modeled PROSAIL surface reflectance to account for a large variety of land targets (200 k spectra). Based on these previous studies, SBAF approach was adapted to calculate the coefficients considering the most range of surface types, such as forest, grassland, water, crops and soil samples. We obtained 25 cloud-free EO-1 Hyperion images from the Earth Explorer site (<http://earthexplorer.usgs.gov/>) across South America (Table A1). All the Hyperion LIT data were processed to surface reflectance using 6SV model and atmospheric parameters from MAIAC_T (only Terra). The basic parameters (angles, time, location) were extracted from Hyperion metadata, and the averaged atmospheric parameters (AOD, CWV, ozone) were computed from MAIAC_T for each scene and date (Table A1). A total of 15,341 spectral profiles were sampled in the Hyperion SR data to compute the specific-band reflectance (Eq. A1). The profiles were interpolated from 10 nm to 1 nm resolution to match the 1-nm sampling interval of the RSR of sensors, and then, the SBAF was calculated using Equation A2. Although Hyperion provides hyperspectral images from 0.4 to 2.4 μm (contiguous 220 channels), we only used the VNIR wavelengths (356–1058 nm) with 70 calibrated bands. The Hyperion SR curves were spectrally weighted by RSR functions to reconstruct the multi-spectral curves for MUX and OLI sensors as follows:

$$\bar{\rho}_{SR}(\lambda_o) = \frac{\int_{\lambda_1}^{\lambda_2} \rho'_{SR}(\lambda_i) \times RSR(\lambda_i) d\lambda}{\int_{\lambda_1}^{\lambda_2} RSR(\lambda_i) d\lambda} \quad (A1)$$

Where $\bar{\rho}_{SR}$ is convolved SR values of the specific-sensor and spectral band (λ_o), ρ'_{SR} is Hyperion SR values centered at λ_i wavelength, RSR is the relative response of the bandpass (λ_1, λ_2) from specific-sensor and spectral band.

The spectral band adjustment factor (SBAF _{λ}) was computed by the ratio of $\bar{\rho}_{SR}$ for OLI and MUX.

$$\text{SBAF}(\lambda_o) = \frac{\bar{\rho}_{SR}^{OLI}(\lambda_o)}{\bar{\rho}_{SR}^{MUX}(\lambda_o)} \quad (\text{A2})$$

Where $\bar{\rho}_{SR}^{OLI}$ and $\bar{\rho}_{SR}^{MUX}$ are the convolved SR values using RSR from OLI and MUX, respectively.

Ideally, the calculation of SBAF is desired for each image acquisition (coincident Hyperion and MUX images), but there is an evident limitation of Hyperion dataset, and we assume that the practical approximation accounts for different land cover types. Since the NDVI is one of the most commonly used remote sensing indices, these adjustment factors were calculated as a function of NDVI (Table. A2). This is a practical way to solve a complex problem because the effects of RSR differences vary according to shape and magnitude of targeted surface. The results are shown rather similar SBAF for blue, green and red bands (differences are up to 5%), while NIR band reaches near 25% of differences for high NDVI. Finally, MUX spectra data were adjusted by multiple the MUX SR versus SBAF (λ_o).

Table A1. List of Hyperion images used in this study. The averaged parameters for each image were used in the atmospheric correction.

Hyperion Scene	Date	Lat (degrees)	Lon (degrees)	AOD (unitless)	CWV (g.cm2)	OZ (cm)	Elevation (m)
EO1H0090602016355110K2	12/20/2016	-0.7233245	-76.3155	0.07	3.87	0.2608	268
EO1H2190692017053110KF	2/22/2017	-13.085428	-43.38617	0.059	4.21	0.2618	438
EO1H2190702016253110K2	9/9/2016	-14.8173165	-43.877175	0.0937*	1.53*	0.2846	460
EO1H2210662016060110PF	2/29/2016	-8.5242665	-46.7548195	0.0242	3.64	0.234	486.65
EO1H2210702016150110KF	5/29/2016	-13.9878585	-47.603821	0.0283	2.6	0.2567	670
EO1H2210712015119110KF	4/29/2015	-15.7363505	-47.726247	0.176	2.96	0.2338	1041
EO1H2210712015289110KF	10/16/2015	-15.935291	-47.7452445	0.0168	2.03	0.269	957
EO1H2210752011272110KT	9/29/2011	-21.783152	-48.8656385	0.101	2.12	0.2647	466
EO1H2210752012225110PZ	8/12/2012	-21.725073	-48.899943	0.029	1.51	0.265	462
EO1H2230682016188110KF	7/6/2016	-11.685777	-50.6097225	0.0373	2.9	0.302	193
EO1H2230802013059110KF	2/28/2013	-29.0304395	-53.8064935	0.0139	1.18	0.262	393
EO1H2240642009207110PF	7/26/2009	-6.128575 -	-50.100683	0.0268	2.74	0.261	459
EO1H2240692015336110KF	12/2/2015	-12.9289885	-52.281935	0.0498	4.35	0.292	349
EO1H2240692016221110KP	8/8/2016	-12.8459785	-52.2570235	0.0928	1.97	0.333	347
EO1H2240692016300110KP	10/26/2016	-12.940532	-52.275409	0.1336	4.48	0.351	349
EO1H2240712015265110KF	9/22/2015	-15.8478535	-52.147547	0.328	2.01	0.293	375
EO1H2250792014170110KF	6/19/2014	-27.2840245	-56.750428	0.015	0.61	0.299	83
EO1H2250812010020110PO	1/20/2010	-31.3847345	-57.728872	0.04026	2.62	0.2651	85
EO1H2260792012341110PF	12/6/2012	-28.304424	-58.9653935	0.0626	4.84	0.2586	42
EO1H2270622016189110K4	7/7/2016	-2.751845 -	-54.8429335	0.201	5.026	0.3008	114
EO1H2270822013154110PF	6/3/2013	-31.9101245	-60.5164225	0.0276	1.21	0.272	25

EO1H2280762016265110KF	9/21/2016	-23.6237175	-60.4145115	0.213	1.89	0.443	148
EO1H2310672016176110P0	6/24/2016	-9.950369	61.7915675	0.0373	4.05	0.275	149
EO1H2320822011336110PQ	12/2/2011	-31.8525975	-69.20197	0.07	0.206	0.3063	2205
EO1H2320822013089110P2	3/30/2013	-31.755198	-69.2988435	0.065	0.412	0.267	2208

Table A2. Spectral band adjustment factor for MUX bands as a function of NDVI. The values in parenthesis are the standard deviation of SBAF.

	Blue (485 nm)	Green (555 nm)	Red (660 nm)	NIR (830 nm)	NDVI
SBAF	0.952 (0.026)	1.015 (0.010)	0.986 (0.013)	0.944 (0.099)	-1.0 to -0.4
	0.961 (0.033)	1.012 (0.011)	0.982 (0.021)	1.037 (0.142)	-0.4 to -0.2
	0.963 (0.037)	1.011 (0.012)	0.971 (0.044)	1.108 (0.118)	-0.2 to 0
	0.977 (0.020)	1.001 (0.007)	0.973 (0.027)	1.084 (0.070)	0 to 0.1
	0.983 (0.015)	1.001 (0.005)	0.965 (0.013)	1.194 (0.092)	0.1 to 0.2
	0.937 (0.079)	1.028 (0.027)	0.964 (0.030)	1.248 (0.057)	0.2 to 1.0

References

- Anderson, T. L., Charlson, R. J., Winker, D. M., Ogren, J. A., & Holmén, K. (2003). Mesoscale variations of tropospheric aerosols. *Journal of the Atmospheric Sciences*, 60(1), 119-136.
- Antoine, D., & Morel, A. (1998). Relative importance of multiple scattering by air molecules and aerosols in forming the atmospheric path radiance in the visible and near-infrared parts of the spectrum. *Applied Optics*, 37(12), 2245-2259.
- Cao, C., De Luccia, F. J., Xiong, X., Wolfe, R., & Weng, F. (2014). Early on-orbit performance of the visible infrared imaging radiometer suite onboard the suomi national polar-orbiting partnership (SNPP) satellite. *IEEE Transactions on Geoscience and Remote Sensing*, 52(2), 1142-1156.
- Chander, Gyanesh et al. Applications of spectral band adjustment factors (SBAF) for cross-calibration. *IEEE Transactions on Geoscience and Remote Sensing*, v. 51, n. 3, p. 1267-1281, 2013.
- Claverie, M., Vermote, E. F., Franch, B., & Masek, J. G. (2015). Evaluation of the Landsat-5 TM and Landsat-7 ETM+ surface reflectance products. *Remote Sensing of Environment*, 169, 390-403.
- Doxani, G., Vermote, E., Roger, J. C., Gascon, F., Adriaensen, S., Frantz, D., ... & Louis, J. (2018). Atmospheric Correction Inter-Comparison Exercise. *Remote Sensing*, 10(2), 352.
- Eck, T. F., Holben, B. N., Reid, J. S., Dubovik, O., Smirnov, A., O'Neill, N. T., ... & Kinne, S. (1999). Wavelength dependence of the optical depth of biomass burning, urban, and desert dust aerosols. *Journal of Geophysical Research: Atmospheres*, 104(D24), 31333-31349.
- Feng, M., Sexton, J. O., Huang, C., Masek, J. G., Vermote, E. F., Gao, F., ... & Townshend, J. R. (2013). Global surface reflectance products from Landsat: Assessment using coincident MODIS observations. *Remote Sensing of Environment*, 134, 276-293.
- Fioletov, V. E. (2008). Ozone climatology, trends, and substances that control ozone. *Atmosphere-Ocean*, 46(1), 39-67.
- Fonseca, L. M., Epiphanyo, J. C. N., Valeriano, D. M., Soares, J. V., Dalge, J. C., & Alvarenga, M. A. (2014). Earth observation applications in Brazil with focus on the CBERS program. *IEEE Geoscience and Remote Sensing Magazine*, 2(2), 53-55.
- Franch, B., Vermote, E. F., & Claverie, M. (2014). Intercomparison of Landsat albedo retrieval techniques and evaluation against in situ measurements across the US SURFRAD network. *Remote Sensing of Environment*, 152, 627-637.
- Fraser, R. S., & Kaufman, Y. J. (1985). The relative importance of aerosol scattering and absorption in remote sensing. *IEEE transactions on geoscience and remote sensing*, (5), 625-633.

- Gao, B. C., Montes, M. J., Davis, C. O., & Goetz, A. F. (2009). Atmospheric correction algorithms for hyperspectral remote sensing data of land and ocean. *Remote Sensing of Environment*, 113, S17-S24.
- Hilker, T., Lyapustin, A. I., Tucker, C. J., Sellers, P. J., Hall, F. G., & Wang, Y. (2012). Remote sensing of tropical ecosystems: Atmospheric correction and cloud masking matter. *Remote Sensing of Environment*, 127, 370-384.
- Hsu, N. C., Jeong, M. J., Bettenhausen, C., Sayer, A. M., Hansell, R., Seftor, C. S., ... & Tsay, S. C. (2013). Enhanced Deep Blue aerosol retrieval algorithm: The second generation. *Journal of Geophysical Research: Atmospheres*, 118(16), 9296-9315.
- Hu, Y., Liu, L., Liu, L., Peng, D., Jiao, Q., & Zhang, H. (2014). A Landsat-5 atmospheric correction based on MODIS atmosphere products and 6S model. *IEEE Journal of Selected Topics in Applied Earth Observations and Remote Sensing*, 7(5), 1609-1615.
- Hubanks, P., Platnick, S., & King, M. (2015). MODIS Atmosphere L3 Gridded Product Algorithm Theoretical Basis Document (ATBD) & Users Guide. ATBDMOD-30, NASA. Retrieved from http://modis-atmos.gsfc.nasa.gov/docs/L3_ATBD_C6_2015_05_06.pdf
- Jackson, J. M., Liu, H., Laszlo, I., Kondragunta, S., Remer, L. A., Huang, J., & Huang, H. C. (2013). Suomi-NPP VIIRS aerosol algorithms and data products. *Journal of Geophysical Research: Atmospheres*, 118(22).
- Jiménez-Muñoz, J. C., Sobrino, J. A., Mattar, C., & Franch, B. (2010). Atmospheric correction of optical imagery from MODIS and Reanalysis atmospheric products. *Remote Sensing of Environment*, 114(10), 2195-2210.
- Ju, J., Roy, D. P., Vermote, E., Masek, J., & Kovalskyy, V. (2012). Continental-scale validation of MODIS-based and LEDAPS Landsat ETM+ atmospheric correction methods. *Remote Sensing of Environment*, 122, 175-184.
- Justice, C. O., Townshend, J. R. G., Vermote, E. F., Masuoka, E., Wolfe, R. E., Saleous, N., ... & Morisette, J. T. (2002). An overview of MODIS Land data processing and product status. *Remote sensing of Environment*, 83(1-2), 3-15.
- Kahn, R. A., Nelson, D. L., Garay, M. J., Levy, R. C., Bull, M. A., Diner, D. J., ... & Remer, L. A. (2009). MISR aerosol product attributes and statistical comparisons with MODIS. *IEEE Transactions on Geoscience and Remote Sensing*, 47(12), 4095-4114.
- Kaufman, Y. J., Tanré, D., Gordon, H. R., Nakajima, T., Lenoble, J., Frouin, R., ... & Teillet, P. M. (1997a). Passive remote sensing of tropospheric aerosol and atmospheric correction for the aerosol effect. *Journal of Geophysical Research: Atmospheres*, 102(D14), 16815-16830.
- Kaufman, Y. J., Wald, A. E., Remer, L. A., Gao, B. C., Li, R. R., & Flynn, L. (1997b). The MODIS 2.1 um channel-correlation with visible reflectance for use in remote sensing of aerosol. *IEEE transactions on Geoscience and Remote Sensing*, 35(5), 1286-1298.
- Kotchenova, S. Y., Vermote, E. F., Matarrese, R., & Klemm Jr, F. J. (2006). Validation of a vector version of the 6S radiative transfer code for atmospheric correction of satellite data. Part I: Path radiance. *Applied optics*, 45(26), 6762-6774.
- Levy, R. C., Remer, L. A., Mattoo, S., Vermote, E. F., & Kaufman, Y. J. (2007). Second-generation operational algorithm: Retrieval of aerosol properties over land from inversion of Moderate Resolution Imaging Spectroradiometer spectral reflectance. *Journal of Geophysical Research: Atmospheres*, 112(D13).
- Levy, R. C., Munchak, L. A., Mattoo, S., Patadia, F., Remer, L. A., & Holz, R. E. (2015). Towards a long-term global aerosol optical depth record: applying a consistent aerosol retrieval algorithm to MODIS and VIIRS-observed reflectance. *Atmospheric Measurement Techniques*, 8(10), 4083-4110.
- Liang, S., Fallah-Adl, H., Kalluri, S., JáJá, J., Kaufman, Y. J., & Townshend, J. R. (1997). An operational atmospheric correction algorithm for Landsat Thematic Mapper imagery over the land. *Journal of Geophysical Research: Atmospheres*, 102(D14), 17173-17186.
- Liang, S., Fang, H., & Chen, M. (2001). Atmospheric correction of Landsat ETM+ land surface imagery. I. Methods. *IEEE Transactions on geoscience and remote sensing*, 39(11), 2490-2498.

- Liang, F., Xiao, Q., Wang, Y., Lyapustin, A., Li, G., Gu, D., ... & Liu, Y. (2018). MAIAC-based long-term spatiotemporal trends of PM_{2.5} in Beijing, China. *Science of The Total Environment*, 616, 1589-1598.
- Liu, H., Remer, L. A., Huang, J., Huang, H. C., Kondragunta, S., Laszlo, I., ... & Jackson, J. M. (2014). Preliminary evaluation of S-NPP VIIRS aerosol optical thickness. *Journal of Geophysical Research: Atmospheres*, 119(7), 3942-3962.
- Lyapustin, A. I. (1999). Atmospheric and geometrical effects on land surface albedo. *Journal of Geophysical Research: Atmospheres*, 104(D4), 4127-4143.
- Lyapustin, A., & Wang, Y. (2009). The time series technique for aerosol retrievals over land from MODIS. In *Satellite aerosol remote sensing over land* (pp. 69-99). Springer, Berlin, Heidelberg.
- Lyapustin, A., Wang, Y., Laszlo, I., Kahn, R., Korkin, S., Remer, L., ... & Reid, J. S. (2011). Multiangle implementation of atmospheric correction (MAIAC): 2. Aerosol algorithm. *Journal of Geophysical Research: Atmospheres*, 116(D3).
- Lyapustin, A. I., Wang, Y., Laszlo, I., Hilker, T., Hall, F. G., Sellers, P. J., ... & Korkin, S. V. (2012). Multi-angle implementation of atmospheric correction for MODIS (MAIAC): 3. Atmospheric correction. *Remote Sensing of Environment*, 127, 385-393.
- Lyapustin, A., Wang, Y., Korkin, S., and Huang, D. (2018). MODIS Collection 6 MAIAC Algorithm, *Atmos. Meas. Tech. Discuss.*, <https://doi.org/10.5194/amt-2018-141>, in review.
- Maiersperger, T. K., Scaramuzza, P. L., Leigh, L., Shrestha, S., Gallo, K. P., Jenkerson, C. B., & Dwyer, J. L. (2013). Characterizing LEDAPS surface reflectance products by comparisons with AERONET, field spectrometer, and MODIS data. *Remote Sensing of Environment*, 136, 1-13.
- Martins, V. S., Barbosa, C. C. F., de Carvalho, L. A. S., Jorge, D. S. F., Lobo, F. D. L., & Novo, E. M. L. D. M. (2017a). Assessment of atmospheric correction methods for Sentinel-2 MSI images applied to Amazon floodplain lakes. *Remote Sensing*, 9(4), 322.
- Martins, V. S., Lyapustin, A., Carvalho, L. A. S., Barbosa, C. C. F., & Novo, E. M. L. M. (2017b). Validation of high-resolution MAIAC aerosol product over South America. *Journal of Geophysical Research: Atmospheres*.
- Martins, V. S., Novo, E. M., Lyapustin, A., Aragão, L. E., Freitas, S. R., & Barbosa, C. C. (2018). Seasonal and interannual assessment of cloud cover and atmospheric constituents across the Amazon (2000–2015): Insights for remote sensing and climate analysis. *ISPRS Journal of Photogrammetry and Remote Sensing*. <https://doi.org/10.1016/j.isprsjprs.2018.05.013> (in press).
- Masek, J. G., Vermote, E. F., Saleous, N. E., Wolfe, R., Hall, F. G., Huemmrich, K. F., ... & Lim, T. K. (2006). A Landsat surface reflectance dataset for North America, 1990-2000. *IEEE Geoscience and Remote Sensing Letters*, 3(1), 68-72.
- Mishra, N., Helder, D., Angal, A., Choi, J., & Xiong, X. (2014). Absolute calibration of optical satellite sensors using Libya 4 pseudo invariant calibration site. *Remote sensing*, 6(2), 1327-1346.
- Muller-Wilm, U., Louis, J., Richter, R., Gascon, F., & Niezette, M. (2013). Sentinel-2 level 2A prototype processor: Architecture, algorithms and first results. In *Proceedings of the ESA Living Planet Symposium*, Edinburgh, UK (pp. 9-13).
- Pinto, C., Ponzoni, F., Castro, R., Leigh, L., Mishra, N., Aaron, D., & Helder, D. (2016a). First in-flight radiometric calibration of MUX and WFI on-board CBERS-4. *Remote Sensing*, 8(5), 405.
- Pinto, C. T., Ponzoni, F. J., Castro, R. M., Leigh, L., Kaewmanee, M., Aaron, D., & Helder, D. (2016b). Evaluation of the uncertainty in the spectral band adjustment factor (SBAF) for cross-calibration using Monte Carlo simulation. *Remote Sensing Letters*, 7(9), 837-846.
- Remer, L. A., Kaufman, Y. J., Tanré, D., Mattoo, S., Chu, D. A., Martins, J. V., ... & Eck, T. F. (2005). The MODIS aerosol algorithm, products, and validation. *Journal of the atmospheric sciences*, 62(4), 947-973.
- Roy, D. P., Qin, Y., Kovalskyy, V., Vermote, E. F., Ju, J., Egorov, A., ... & Yan, L. (2014a). Conterminous United States demonstration and characterization of MODIS-based Landsat ETM+ atmospheric correction. *Remote Sensing of Environment*, 140, 433-449.

- Roy, D. P., Wulder, M. A., Loveland, T. R., Woodcock, C. E., Allen, R. G., Anderson, M. C., ... & Scambos, T. A. (2014b). Landsat-8: Science and product vision for terrestrial global change research. *Remote sensing of Environment*, 145, 154-172.
- Seemann, S. W., Li, J., Menzel, W. P., & Gumley, L. E. (2003). Operational Retrieval of Atmospheric Temperature, Moisture, and Ozone from MODIS Infrared Radiances. *Journal of Applied Meteorology*, 42, 1072–1091. [http://doi.org/10.1175/1520-0450\(2003\)042<1072:OROATM>2.0.CO;2](http://doi.org/10.1175/1520-0450(2003)042<1072:OROATM>2.0.CO;2)
- Steven, M. D., Malthus, T. J., Baret, F., Xu, H., & Chopping, M. J. (2003). Intercalibration of vegetation indices from different sensor systems. *Remote Sensing of Environment*, 88(4), 412-422.
- Superczynski, S. D., Kondragunta, S., & Lyapustin, A. I. (2017). Evaluation of the multi-angle implementation of atmospheric correction (MAIAC) aerosol algorithm through intercomparison with VIIRS aerosol products and AERONET. *Journal of Geophysical Research: Atmospheres*, 122(5), 3005-3022.
- Tanré, D., Herman, M., Deschamps, P. Y., & De Lefte, A. (1979). Atmospheric modeling for space measurements of ground reflectances, including bidirectional properties. *Applied optics*, 18(21), 3587-3594.
- Tanré, D., Herman, M., & Deschamps, P. Y. (1981). Influence of the background contribution upon space measurements of ground reflectance. *Applied Optics*, 20(20), 3676-3684.
- Taylor, M.; Kazadzis, S.; Amiridis, V.; Kahn, R.A. Global aerosol mixtures and their multiyear and seasonal characteristics. *Atmos. Environ.* 2015, 116, 112–129.
- Vermote, E. F., Tanré, D., Deuze, J. L., Herman, M., & Morcette, J. J. (1997). Second simulation of the satellite signal in the solar spectrum, 6S: An overview. *IEEE transactions on geoscience and remote sensing*, 35(3), 675-686.
- Vermote, E. F., El Saleous, N. Z., & Justice, C. O. (2002). Atmospheric correction of MODIS data in the visible to middle infrared: first results. *Remote Sensing of Environment*, 83(1-2), 97-111.
- Vermote, E. F., & Kotchenova, S. (2008). Atmospheric correction for the monitoring of land surfaces. *Journal of Geophysical Research: Atmospheres*, 113(D23).
- Vermote, E., Justice, C., Claverie, M., & Franch, B. (2016). Preliminary analysis of the performance of the Landsat 8/OLI land surface reflectance product. *Remote Sensing of Environment*, 185, 46-56.
- Vicente-Serrano, S. M., Pérez-Cabello, F., & Lasanta, T. (2008). Assessment of radiometric correction techniques in analyzing vegetation variability and change using time series of Landsat images. *Remote Sensing of Environment*, 112(10), 3916-3934.
- Vuolo, F., Mattiuzzi, M., & Atzberger, C. (2015). Comparison of the Landsat Surface Reflectance Climate Data Record (CDR) and manually atmospherically corrected data in a semi-arid European study area. *International Journal of Applied Earth Observation and Geoinformation*, 42, 1-10.
- Wang, Y., Lyapustin, A. I., Privette, J. L., Morisette, J. T., & Holben, B. (2009). Atmospheric correction at AERONET locations: A new science and validation data set. *IEEE Transactions on Geoscience and Remote Sensing*, 47(8), 2450-2466.
- Wang, Y., Liu, L., Hu, Y., Li, D., & Li, Z. (2016). Development and validation of the Landsat-8 surface reflectance products using a MODIS-based per-pixel atmospheric correction method. *International Journal of Remote Sensing*, 37(6), 1291-1314.
- Wilson, R. T. (2013). Py6S: A Python interface to the 6S radiative transfer model. *Computers & Geosciences*, 51(2), 166.
- Zelazowski, P., Sayer, A. M., Thomas, G. E., & Grainger, R. G. (2011). Reconciling satellite-derived atmospheric properties with fine-resolution land imagery: Insights for atmospheric correction. *Journal of Geophysical Research: Atmospheres*, 116(D18).
- Zhang, H. K., Roy, D. P., Yan, L., Li, Z., Huang, H., Vermote, E., ... & Roger, J. C. (2018). Characterization of Sentinel-2A and Landsat-8 top of atmosphere, surface, and nadir BRDF adjusted reflectance and NDVI differences. *Remote Sensing of Environment*.

Ziemke, J. R., Chandra, S., Labow, G. J., Bhartia, P. K., Froidevaux, L., & Witte, J. C. (2011). A global climatology of tropospheric and stratospheric ozone derived from Aura OMI and MLS measurements. *Atmospheric Chemistry and Physics*, 11(17), 9237-9251.

List of Figure Captions

Figure 1. Relative spectral response of CBERS-4 MUX (solid line) and Landsat 8 OLI (dashed line) for the bands used in this study.

Figure 2. Coupled moderate atmospheric products for aerosol and water vapor at August 22th, 2015. The MUX Level-4 scenes illustrate the overlay of atmospheric products in this day.

Figure 3. Flowchart for MUX surface reflectance retrievals and its evaluation.

Figure 4. Spatial distribution of the number of selected images used in the inter-comparison MUX and OLI surface reflectance within 2015-2016 period. The AERONET sites are shown in the bottom-right list.

Figure 5. Scatter plots of MUX (y-axis) and AERONET-derived (x-axis) surface reflectance data for all spectral bands. The AERONET-derived SR, or reflectance truth, is obtained by correcting the TOA reflectance of MUX using AERONET as input for aerosol and water vapor. The statistical metrics are linear regression equation, correlation coefficient (R), number of samples (n), root-mean-square-deviation (RMSD), mean difference (BIAS), and relative error (RE).

Figure 6. The number of coincident MUX and OLI images used in this study (2015-2016).

Figure 7. True color composite of the MUX bands using raw digital number (left) and surface reflectance (right) at September 28, 2016. These images are displayed with the same stretch for RGB bands (no contrast or histogram handle).

Figure 8. Scatter plots of MUX (y-axis) and OLI (x-axis) surface reflectance data for all bands. The statistical metrics are described in the right-bottom text as follows: number of samples (n), root-mean-square-deviation (RMSD), and mean difference (BIAS). The boxplots show mean difference between MUX and OLI (y-axis) as a function of surface reflectance (x-axis). The box edge represents 25 and 75%; whiskers are 5 – 95%; and the central line (blue color) and dot (red color) are median and mean, respectively.

Figure 9. Example of MUX and OLI surface reflectance acquired on August 9 2015. The histogram distribution of surface reflectance shows similarities between sensor products.

Figure 10. Time series NDVI profile coupling MUX and OLI SR data at Central-West region, Brazil. This result is shown the potential application of integrated data. Note that x-axis is irregular in chronological time, and the adjusted curve was obtained from Savitzky–Golay filter.